

Towards Kriging-informed Conditional Diffusion for Regional Sea-Level Data Downscaling

Subhankar Ghosh*

ghosh117@umn.edu

University of Minnesota, Twin Cities
Minneapolis, Minnesota, USA

Arun Sharma*

sharm485@umn.edu

University of Minnesota, Twin Cities
Minneapolis, Minnesota, USA

Jayant Gupta

jayant.j.gupta@oracle.com
Oracle Inc.
USA

Aneesh Subramanian

aneeshcbs@colorado.edu

University of Colorado, Boulder
Boulder, Colorado, USA

Shashi Shekhar

shekhar@umn.edu

University of Minnesota, Twin Cities
Minneapolis, Minnesota, USA

Abstract

Given coarser-resolution projections from global climate models or satellite data, the downscaling problem aims to estimate finer-resolution regional climate data, capturing fine-scale spatial patterns and variability. Downscaling is any method to derive high-resolution data from low-resolution variables, often to provide more detailed and local predictions and analyses. This problem is societally crucial for effective adaptation, mitigation, and resilience against significant risks from climate change. The challenge arises from spatial heterogeneity and the need to recover finer-scale features while ensuring model generalization. Most downscaling methods [23] fail to capture the spatial dependencies at finer scales and underperform on real-world climate datasets, such as sea-level rise. We propose a novel Kriging-informed Conditional Diffusion Probabilistic Model (Ki-CDPM) to capture spatial variability while preserving fine-scale features. Experimental results on climate data show that our proposed method is more accurate than state-of-the-art downscaling techniques.

CCS Concepts

• Computing methodologies → Spatial and physical reasoning; Appearance and texture representations; Machine learning approaches.

Keywords

Remote Sensing, GeoAI, Climate Science, Geostatistics, Generative AI, Downscaling, Diffusion Models, Kriging

*Subhankar Ghosh and Arun Sharma contributed equally to this paper.

Permission to make digital or hard copies of all or part of this work for personal or classroom use is granted without fee provided that copies are not made or distributed for profit or commercial advantage and that copies bear this notice and the full citation on the first page. Copyrights for components of this work owned by others than the author(s) must be honored. Abstracting with credit is permitted. To copy otherwise, or republish, to post on servers or to redistribute to lists, requires prior specific permission and/or a fee. Request permissions from permissions@acm.org.

SIGSPATIAL '24, October 29-November 1, 2024, Atlanta, GA, USA

© 2024 Copyright held by the owner/author(s). Publication rights licensed to ACM.

ACM ISBN 979-8-4007-1107-7/24/10...\$15.00

<https://doi.org/10.1145/3678717.3691304>

ACM Reference Format:

Subhankar Ghosh, Arun Sharma, Jayant Gupta, Aneesh Subramanian, and Shashi Shekhar. 2024. Towards Kriging-informed Conditional Diffusion for Regional Sea-Level Data Downscaling. In *The 32nd ACM International Conference on Advances in Geographic Information Systems (SIGSPATIAL '24), October 29-November 1, 2024, Atlanta, GA, USA*. ACM, New York, NY, USA, 12 pages. <https://doi.org/10.1145/3678717.3691304>

1 Introduction

Given coarse-resolution climate projections from global climate models or satellite data, the problem of statistical downscaling aims to estimate high-resolution regional climate data, capturing fine-scale spatial patterns and variability for a climate variable (e.g., sea-level rise). Since downscaling generates high-resolution data from low-resolution variables, statistical downscaling uses statistical methods to establish relationships between coarse-resolution climate data and high-resolution historical observations. For instance, Figure 1 shows a geographic area near Ecuador and Peru in two different time frames. In both images, the blurry coarse-resolution projections display limited variation in sea surface height anomalies compared to the fine-scale resolution, as shown in the rectangular strips (in red). The ability to capture localized variations is crucial for accurately predicting climate change effects (e.g., sea-level rise) in a specific area.

The regional downscaling problem is vital for developing comprehensive climate policies and strategies. The impacts of climate change, as predicted by global climate models, range from extreme weather events to rises in sea levels and shifts in agricultural productivity. Enhancing the spatial precision of climate data is vital for accurately assessing risks in specific regions. Decision-makers require such information to strategize how communities can successfully mitigate and adapt to these threats. For example, coastal areas worldwide face severe risks associated with sea-level rise, where even small changes can lead to significant flooding, erosion, and habitat loss [16, 32]. High-resolution data contributes to accurate regional predictions of this risk, essential for effective coastal management, infrastructure planning, and disaster preparedness.

The problem of statistical downscaling in climate data is challenging due to climate data's inherent complexity and variability involving intricate spatial and temporal dependencies influenced

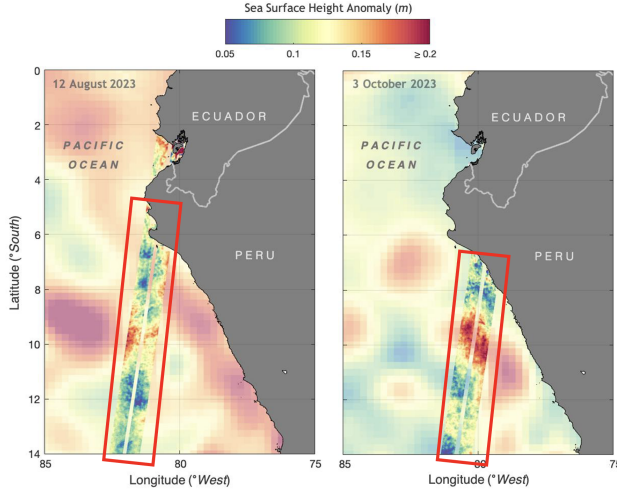


Figure 1: An illustrative example of differentiating coarse resolution and fine-scale resolution observations [35]. (Best in color)

Table 1: Applications of the Data Downscaling Problem

Application Domain	Occurrence of Spatial Variability
Temperature	Regional Temperature Change Prediction
Soil Carbon Emission	Local Farmland Emission vs Global
Precipitation	Regional variability in precipitation
Extreme wind	Regional wind variability (e.g., wind farms)
Climate Policy Making	County vs State level jurisdictions.

by numerous physical processes (e.g., ocean currents, wind patterns, temperature gradients, and coastal topography). The non-stationarity of climate data, driven by dynamic changes in climate patterns and extreme events, further complicates the development of reliable and robust downscaling techniques. For example, statistical properties like mean and standard deviation may not be constant over time [3, 25].

Traditional Kriging and interpolation-based methods [27, 46, 50] for downscaling sea-level rise data often fall short due to their reliance on stationarity assumptions and their inability to capture the dynamic nature of climate data. These methods typically smooth the data excessively, resulting in the loss of critical fine-scale features. The loss leads to an inaccurate representation of the underlying physical processes, such as ocean currents, wind patterns, and temperature gradients. On the other hand, machine learning-based methods [22, 51, 53], while powerful in capturing non-linear relationships, often struggle with generalization and maintaining physical consistency. These models can be data-hungry and sensitive to the quality and quantity of training data.

Traditional super-resolution models, designed primarily for image processing, cannot be directly applied to climate downscaling for the following reasons. (a) They lack physical constraints and fail to incorporate the complex, nonlinear relationships between various components of the Earth system [5, 31]. (b) They do not handle the high-dimensional nature of climate data effectively and often require large amounts of high-resolution training data, typically sparse in climate science [52]. (c) They are deterministic and do not provide probabilistic outputs or uncertainty estimates, which are crucial for climate predictions [28]. (d) They lack generalization

across different regions and periods, as they do not account for the multiple scales inherent in climate processes [21].

To address these limitations, we propose a Kriging-informed Conditional Diffusion Probabilistic Model (Ki-CDPM), which combines the strengths of Kriging's spatial interpolation capabilities with the flexibility and robustness of conditional diffusion processes. Ki-CDPM effectively captures spatial variability, maintains physical consistency, handles high-dimensional data, and provides probabilistic outputs, ensuring more accurate and physically consistent downscaling of climate data.

Table 2: Comparison of methods for sea-level downscaling

	ML based methods	
	No	Yes
Kriging (spatial variability)		
No	x	[22, 51, 53]
Yes	[27, 46, 50]	Ki-CDPM

Contributions: The paper contributions are as follows:

- We propose a novel Kriging-informed Conditional Diffusion Probabilistic Model (Ki-CDPM) that leverages Kriging interpolation for fine-scale projections.
- We introduce Variogram-Based Regularization to capture spatial variability in regional processes and enhance the physical consistency of downscaled data.
- We compare the Ki-CDPM against state-of-the-art machine learning models and conduct comprehensive evaluations in different regions, demonstrating its effectiveness.

Relevance to SIGSPATIAL: This paper is relevant to SIGSPATIAL for the following reasons:

- The paper proposes a novel approach to addressing the challenge of downscaling climate data, which aligns with the fields of remote sensing, earth observation, spatial data mining, and knowledge discovery
- Models used in the paper (e.g., diffusion models) have been explored recently in SIGSPATIAL with promising results in graph forecasting [54] and urban flow [55].
- Challenges described in the paper (e.g., spatial variability) have been studied recently in SIGSPATIAL (e.g., [24]).
- The paper integrates geostatistical methods and deep learning models, aligning with SIGSPATIAL's focus on GeoAI.

Scope: This paper focuses on the statistical downscaling of climate variables like sea-level rise and ocean eddy energy. Temporal downscaling is not addressed in this manuscript but will be explored in future work. This study does not explore physics-informed machine-learning methods for downscaling or does not simulate the temporal evolution of physical processes. Additional physical constraints can be added to the proposed method to explore downscaling climate variables with conservation properties.

Organization: The paper is organized as follows: Section 2 introduces basic concepts and provides the problem formulation. Section 3 describes the overall architecture of the Kriging-informed Conditional Diffusion Probabilistic Model (Ki-CDPM) and the variogram-based regularization. Experimental evaluations are presented for the proposed approach in Section 4. Related work is mentioned in Section 5. Finally, Section 6 concludes this work and briefly lists the future work.

2 Problem Formulation

2.1 Basic Concepts

DEFINITION 2.1. *A Sea-Level Rise or Sea-Level Elevation Map* is a raster map that provides information on the average increase in the water level of the Earth's oceans. Sea level is the height of the sea surface relative to a standardized baseline, typically the mean sea level. It is measured using satellite altimetry, tide gauges, and GPS data, which require advanced algorithms for integrating and correcting various environmental factors. Understanding sea level elevation is crucial for climate research, disaster management, and urban planning and involves complex data processing, modeling, and predictive analytics [10].

Figure 1 shows sea-level rise information for the eastern equatorial Pacific Ocean and coastal Peru and Ecuador regions, where red and green contours depict high and low sea-level rise, respectively. From the coarse scale resolution (background color), we can observe that sea-level elevation along this coastal region was higher in August 2023 than in October 2023.

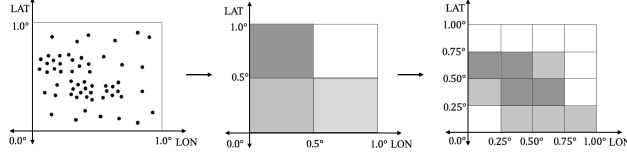


Figure 2: Coarse-scale and fine-scale resolution example.

DEFINITION 2.2. *A coarse-scale resolution* is a $N \times N$ grid-based representation of a climate variable (e.g., sea-level elevation) for a given geographic region (R) projection.

Figure 2 shows a study area with a $1^\circ \times 1^\circ$ spatial resolution, containing randomly distributed data points that were later discretized to a $0.5^\circ \times 0.5^\circ$ resolution, revealing variations in population density.

DEFINITION 2.3. *A fine-scale resolution* is an $M \times M$ (where $M > N$) grid-based representation of a climate variable (e.g., sea-level elevation) for a given geographic region (R) projection.

Figure 2(c) shows a study area with a spatial resolution of $0.25^\circ \times 0.25^\circ$ revealing finer scale variations in population density.

DEFINITION 2.4. *Downscaling* in climate science derives fine-scale resolution data from coarse-resolution variables [25].

Figure 3 shows the down-scaling process for a real-world temperature heatmap. Spatial variability within the map can be observed between the northern and the southern regions. Further, it is observed that the finer resolution data is better for observing regional patterns (e.g., Regions to the West of the center).

2.2 Problem Formulation

The problem of downscaling a climate variable (e.g., sea-level elevation) is formally defined as follows:

Input:

- (1) Coarse-Resolution climate data (\tilde{y})
- (2) A diffusion model to output a downsampled climate dataset (\tilde{x}_{high}) which is an approximation of the ground truth (x_{high})

Output: High-resolution downsampled climate data (\tilde{x}_{high}) as an approximation of the ground truth data (x_{high})

Objective: Solution quality, model generalization

Constraints: (1) Spatial variability; (2) Domain adaptability; (3) Model interpretability

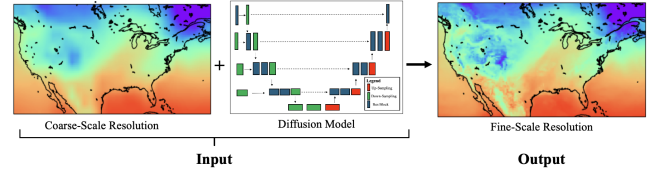


Figure 3: An illustrative example of input and output (Maps adapted from [53]).

Inverse Problem: Downscaling sea-level rise projections from coarse-resolution climate models to finer regional scales can be thought of as an inverse problem aimed at estimating high-resolution sea-level changes based on limited low-resolution observations and a forward model [18, 25]. This problem is complex due to nonlinear relationships between inputs and outputs, sparse and unevenly distributed observations, and model errors and uncertainties [3, 5, 31, 40]. Additionally, the high-dimensional nature of the problem poses computational challenges [21]. These factors make sea-level rise data downscaling an ill-posed inverse problem, which requires advanced techniques for reliable high-resolution projections [28, 52].

3 Kriging-informed Conditional Diffusion

Probabilistic Model

This section will introduce a novel architecture based on Kriging interpolation as a conditional input to preserve spatial variability while transforming coarser-resolution climate variables (e.g., sea-level elevation) to finer-scale resolution. Section 3.3 provides a detailed explanation of the proposed architecture, and Section 3.4 shows the Kriging-informed training and regularization.

3.1 Conditional Diffusion Probabilistic Model

In this approach, the goal is to generate a fine-scale resolution map from a coarse-resolution input map in which samples were drawn from an unknown conditional distribution $p(\mathbf{x} | \mathbf{y})$ where $p(\mathbf{y})$ is a distribution of Kriging-interpolated map of the coarse-scale resolution input (\tilde{y}). The objective is to learn a parametric approximation of $p(\mathbf{x} | \mathbf{y})$ via stochastic refinements which iteratively maps source condition \mathbf{y} to a target output $\mathbf{x} \in \mathbb{R}^d$ via denoising diffusion probabilistic (DDPM) model [14, 41].

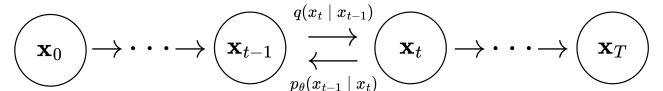


Figure 4: Forward and Reverse Diffusion Processes

Figure 4 presents a detailed view of a diffusion model where isotropic Gaussian noise is progressively added to a signal through a predetermined Markov chain, denoted by $q(\mathbf{x}_t | \mathbf{x}_{t-1})$. This process generates a series of intermediate noisy maps referred to as *forward* diffusion. Conversely, in *reverse* diffusion, the process begins with a completely noisy map, $\mathbf{x}_T \sim \mathcal{N}(\mathbf{0}, \mathbf{I})$. The model then incrementally refines this map through successive iterations ($\mathbf{x}_{T-1}, \mathbf{x}_{T-2}, \dots, \mathbf{x}_0$) using **learned conditional transition distributions** $p_\theta(\mathbf{x}_{t-1} |$

Algorithm 1 Training

```

1: repeat
2:    $(\mathbf{x}_0, \mathbf{y}) \sim p(\mathbf{x}, \mathbf{y})$ 
3:    $\psi \sim p(\psi)$ 
4:    $\epsilon \sim \mathcal{N}(\mathbf{0}, \mathbf{I})$ 
5:   Take a gradient descent step on
        $\nabla_{\theta} \left\| \epsilon - f_{\theta}(\mathbf{y}, \sqrt{\psi} \mathbf{x}_0 + \sqrt{1 - \psi} \epsilon, \psi) \right\|_p^p$ 
6: until converged

```

\mathbf{x}_t, \mathbf{y} , aiming for $\mathbf{x}_0 \sim p(\mathbf{x} | \mathbf{y})$. This method reverses the forward diffusion process by reconstructing the signal from noise using a backward Markov chain conditioned on \mathbf{y} .

Forward Process (q): In this process, gaussian noise is progressively added to a fine-scale resolution \mathbf{x}_0 over T iterations [14, 41]:

$$q(\mathbf{x}_{1:T} | \mathbf{x}_0) = \prod_{t=1}^T q(\mathbf{x}_t | \mathbf{x}_{t-1}), \quad (1)$$

$$q(\mathbf{x}_t | \mathbf{x}_{t-1}) = \mathcal{N}(\mathbf{x}_t | \sqrt{\alpha_t} \mathbf{x}_{t-1}, (1 - \alpha_t) \mathbf{I}), \quad (2)$$

Here, the hyperparameters $\alpha_{1:T}$ are constrained between 0 and 1, representing the noise variance introduced at each iteration. The variable \mathbf{x}_{t-1} is scaled down by a factor of $\sqrt{\alpha_t}$ to keep the variance of the random variables finite. Additionally, deriving \mathbf{x}_t from \mathbf{x}_0 can be streamlined using Equation 3.:

$$q(\mathbf{x}_t | \mathbf{x}_0) = \mathcal{N}(\mathbf{x}_t | \sqrt{\psi_t} \mathbf{x}_0, (1 - \psi_t) \mathbf{I}), \quad (3)$$

where $\psi_t = \prod_{i=1}^t \alpha_i$. In addition, one can derive the posterior distribution of \mathbf{x}_{t-1} given $(\mathbf{x}_0, \mathbf{x}_t)$ as

$$\begin{aligned} q(\mathbf{x}_{t-1} | \mathbf{x}_0, \mathbf{x}_t) &= \mathcal{N}(\mathbf{x}_{t-1} | \mu, \sigma^2 \mathbf{I}) \\ \mu &= \frac{\sqrt{\psi_{t-1}} (1 - \alpha_t)}{1 - \psi_t} \mathbf{x}_0 + \frac{\sqrt{\alpha_t} (1 - \psi_{t-1})}{1 - \psi_t} \mathbf{x}_t \\ \sigma^2 &= \frac{(1 - \psi_{t-1})(1 - \alpha_t)}{1 - \psi_t}. \end{aligned} \quad (4)$$

Reverse Process (p_{θ}): In this process, we leverage additional kriging interpolated source elevation map \mathbf{y} and optimize a neural denoising model f_{θ} that takes as input map \mathbf{y} and a noisy map $\tilde{\mathbf{x}}$,

$$\tilde{\mathbf{x}} = \sqrt{\psi} \mathbf{x}_0 + \sqrt{1 - \psi} \epsilon, \quad \epsilon \sim \mathcal{N}(\mathbf{0}, \mathbf{I}), \quad (5)$$

Equation 5 aims to restore the noise-free target map \mathbf{x}_0 , and $\tilde{\mathbf{x}}$ aligns with the marginal distribution of noisy maps at various stages of the forward diffusion process described in (3).

In contrast to the forward process q , p_{θ} goes in the reverse direction starting from Gaussian noise \mathbf{x}_T :

$$p_{\theta}(\mathbf{x}_0 | \mathbf{y}) = p(\mathbf{x}_T) \prod_{t=1}^T p_{\theta}(\mathbf{x}_{t-1} | \mathbf{x}_t, \mathbf{y}) \quad (6)$$

$$p(\mathbf{x}_T) = \mathcal{N}(\mathbf{x}_T | \mathbf{0}, \mathbf{I}) \quad (7)$$

$$p_{\theta}(\mathbf{x}_{t-1} | \mathbf{x}_t, \mathbf{y}) = \mathcal{N}(\mathbf{x}_{t-1} | \mu_{\theta}(\mathbf{y}, \mathbf{x}_t, \psi_t), \sigma_t^2 \mathbf{I}). \quad (8)$$

The inference process is defined using isotropic Gaussian conditional distributions, $p_{\theta}(\mathbf{x}_{t-1} | \mathbf{x}_t, \mathbf{y})$, that are learned. If the noise variance in the forward process steps is minimized, *i.e.*, $\alpha_{1:T} \approx 1$, the resulting optimal reverse process $p(\mathbf{x}_{t-1} | \mathbf{x}_t, \mathbf{y})$ will closely approximate a Gaussian distribution [41]. The Gaussian conditionals selected for the inference process in (8) can closely approximate the actual reverse process. Moreover, it is necessary for $1 - \psi_T$ to be large enough to ensure that the distribution of \mathbf{x}_T closely aligns with the prior distribution $p(\mathbf{x}_T) = \mathcal{N}(\mathbf{x}_T | \mathbf{0}, \mathbf{I})$, which is a standard Gaussian distribution with mean zero and identity covariance matrix. Here we designed f_{θ} to predict ϵ from any noisy map $\tilde{\mathbf{x}}$,

Algorithm 2 Inference

```

1:  $\mathbf{x}_T \sim \mathcal{N}(\mathbf{0}, \mathbf{I})$ 
2: for  $t = T, \dots, 1$  do
3:    $\mathbf{z} \sim \mathcal{N}(\mathbf{0}, \mathbf{I})$  if  $t > 1$ , else  $\mathbf{z} = \mathbf{0}$ 
4:    $\mathbf{x}_{t-1} = \frac{1}{\sqrt{\alpha_t}} \left( \mathbf{x}_t - \frac{1 - \alpha_t}{\sqrt{1 - \psi_t}} f_{\theta}(\mathbf{y}, \mathbf{x}_t, \psi_t) \right) + \sqrt{1 - \alpha_t} \mathbf{z}$ 
5: return  $\mathbf{x}_0$ 

```

including \mathbf{x}_t . Consequently, we can estimate \mathbf{x}_0 by rearranging the terms as shown in (5):

$$\hat{\mathbf{x}}_0 = \frac{1}{\sqrt{\psi_t}} \left(\mathbf{x}_t - \sqrt{1 - \psi_t} f_{\theta}(\mathbf{y}, \mathbf{x}_t, \psi_t) \right). \quad (9)$$

Finally, we insert $\hat{\mathbf{x}}_0$ into the posterior distribution of $q(\mathbf{x}_{t-1} | \mathbf{x}_0, \mathbf{x}_t)$, which parameterizes the mean of $p_{\theta}(\mathbf{x}_{t-1} | \mathbf{x}_t, \mathbf{y})$ in Equation 10. We set the variance of $p_{\theta}(\mathbf{x}_{t-1} | \mathbf{x}_t, \mathbf{y})$ to $(1 - \alpha_t)$, which is the default variance as determined by the variance of the forward process [14]:

$$\mu_{\theta}(\mathbf{y}, \mathbf{x}_t, \psi_t) = \frac{1}{\sqrt{\alpha_t}} \left(\mathbf{x}_t - \frac{1 - \alpha_t}{\sqrt{1 - \psi_t}} f_{\theta}(\mathbf{y}, \mathbf{x}_t, \psi_t) \right), \quad (10)$$

Additionally, we carry out iterative refinement at each iteration as described in Equation 11 (where $\epsilon_t \sim \mathcal{N}(0, 1)$):

$$\mathbf{x}_{t-1} \leftarrow \frac{1}{\sqrt{\alpha_t}} \left(\mathbf{x}_t - \frac{1 - \alpha_t}{\sqrt{1 - \psi_t}} f_{\theta}(\mathbf{y}, \mathbf{x}_t, \psi_t) \right) + \sqrt{1 - \alpha_t} \epsilon_t, \quad (11)$$

3.2 Interpolation with Kriging

Universal Kriging (U-Krig) is an advanced geostatistical method that allows for interpolation by accounting for deterministic trends and spatial correlation in the data. For instance, let \tilde{y} represent a coarser resolution map and y represent a finer resolution map. We then model the trend using a second-order polynomial function of the spatial coordinates:

$$m(s) = \beta_0 + \beta_1 x + \beta_2 y + \beta_3 x^2 + \beta_4 y^2 + \beta_5 xy \quad (12)$$

Where x and y are the spatial coordinates (longitude and latitude), and $\beta_0, \beta_1, \beta_2, \beta_3, \beta_4, \beta_5$ are the coefficients to be estimated. Hence, the residuals $\gamma(s_i)$ are calculated by subtracting the estimated trend $m(s)$ from the observed sea-level elevations $\tilde{y}(s_i)$:

$$\gamma(s_i) = \tilde{y}(s_i) - m(s_i) \quad (13)$$

These residuals represent the deviations from the deterministic trend and are used to model the spatial correlation structure.

We then use the spatial correlation of the residuals, which is quantified using the *experimental* variogram. The semivariance $\Delta(h)$ for different lag distances h is computed as:

$$\Delta(h) = \frac{1}{2N(h)} \sum_{i=1}^{N(h)} [\gamma(s_i) - \gamma(s_i + h)]^2 \quad (14)$$

Where $N(h)$ is the number of pairs of points separated by a distance h , and $\gamma(s_i)$ are the residuals. The experimental variogram is fitted with a theoretical Matérn variogram model, defined as:

$$\Delta(h) = \sigma^2 \left[1 - \frac{2^{1-v}}{\Gamma(v)} \left(\frac{h}{\rho} \right)^v K_v \left(\frac{h}{\rho} \right) \right] + C_0 \quad (15)$$

where v is the smoothness parameter, ρ is the range parameter, σ^2 is the partial sill, C_0 is the nugget, and K_v is the modified Bessel function of the second kind. Once the variogram parameters (v, ρ, σ^2, C_0) are estimated by fitting the Matérn variogram model to the experimental variogram, they are used to calculate the semivariances $\Delta(s_i - s_j)$ between all pairs of sampled locations. These semivariances form the basis of the Kriging system of equations. We use the Universal Kriging system to predict the sea-level elevation at unsampled locations with a higher resolution. The predicted value $y(s_0)$ at location s_0 is given by:

$$y(s_0) = \sum_{i=1}^n \lambda_i \tilde{y}(s_i) + \sum_{k=1}^p \mu_k f_k(s_0) \quad (16)$$

where λ_i are the Kriging weights, μ_k are the Lagrange multipliers for the trend functions, and $f_k(s_0)$ are the basis functions for the trend model. The weights λ_i are obtained by solving the system of equations:

$$\begin{cases} \sum_{j=1}^n \lambda_j \Delta(s_i - s_j) + \sum_{k=1}^p \mu_k f_k(s_i) = \Delta(s_i - s_0) & \text{for } i = 1, \dots, n \\ \sum_{j=1}^n \lambda_j f_k(s_j) = f_k(s_0) & \text{for } k = 1, \dots, p \end{cases}$$

where $\Delta(s_i - s_j)$ is the semivariance between locations s_i and s_j . Finally, we apply the Universal Kriging weights to interpolate the sea-level elevation data to a higher resolution. This interpolated map y is used as a conditional input to the diffusion model, which then controls the generation in the reverse diffusion process to retain the spatial dependencies.

3.3 Proposed Model Architecture

The Ki-CDPM extends the CDPM by incorporating a conditioned input obtained from Universal-Kriging (U-Krig) on the coarse-resolution elevation map $\tilde{y} \in \mathbb{R}^{M \times M}$ providing local variability for the climate variable. The objective is to find an interpolated elevation map $y \in \mathbb{R}^{N \times N}$ (where $N > M$) with the exact resolution as x_0 . Hence, y is later used as a conditional input concatenated with the noisy elevation map $x_t \in \mathbb{R}^{N \times N}$ at each diffusion step t along the channel dimension, forming a multi-channel input tensor $[x_t, y] \in \mathbb{R}^{N \times N \times 2}$.

The concatenated input tensor is fed into the U-Net [34] architecture of the Ki-CDPM, allowing the model to learn the conditional distribution $p_\theta(x_{t-1}|x_t, y)$. The U-Net can leverage the spatially variable information provided by the U-Krig-based elevation map y to guide the generation of a fine-scale resolution map capturing spatial dependencies via leveraging the strengths of geostatistical information into the diffusion modeling framework.

Execution Trace: Figure 5 provides an overview of our proposed Ki-CDPM, a single conditional diffusion model that utilizes Kriging interpolated elevation map as conditional input y . The forward process begins by adding small Gaussian noise until the input map is completely distorted. In *reverse* process, x_T (i.e., complete random noise) is denoised until we recover \tilde{x}_0 (an approximation of x_0) and within each transition interval, we learn U-Net parameters which allow conditioning with Kriging-interpolated elevation map y to generate finer-scale resolution map. For instance, Figure 5 (a) shows a transition interval x_t and x_{t-1} where the *forward* process is $\in q(x_t|x_{t-1})$ and the *reverse* process is $\in p_\theta(x_{t-1}|x_t, y)$. At time step t , we concatenate the noisy map (x_t) with the U-Krig interpolated

map (y) as a conditional input (where $y \in \mathbb{R}^{N \times N}$) and pass it to the U-Net (as shown in Figure 5 (b)). Thus the *reverse* process is represented by $p_\theta(x_{t-1}|x_t, y)$. In the U-net encoder, we utilize different scales of the conditional input (y) via several stacked down-sampling layers. The U-Net outputs x_{t-1} , a less noisy version of the elevation map. Finally, this process yields the denoised version or a more fine-scale map as the output. For our training noise schedule, we use a piecewise distribution [2], i.e., $p(\psi) = \sum_{t=1}^T \frac{1}{T} U(\psi_{t-1}, \psi_t)$, where we first uniformly sample a time step $t \sim 0, \dots, T$, followed by $\psi \sim U(\psi_{t-1}, \psi_t)$ with $T = 1000$.

3.4 Proposed Variogram-based Regularization

Variational Lower Bound (\mathcal{L}_{VLB}): Considering the forward diffusion process as a set approximate posterior within the inference mechanism, it is possible to establish the ensuing variational lower bound for the marginal log-likelihood:

$$\begin{aligned} \mathbb{E}_{(x_0, y)} \log p_\theta(x_0|y) &\geq \mathbb{E}_{y, x_0} \mathbb{E}_{q(x_{1:T}|x_0)} \left[\log p(x_T) \right. \\ &\quad \left. + \sum_{t \geq 1} \log \frac{p_\theta(x_{t-1}|x_t, y)}{q(x_t|x_{t-1})} \right] \end{aligned} \quad (17)$$

According to the specific parameterization of the inference process described earlier, the negative variational lower bound can be simplified and expressed as a loss function. This simplified loss consists of terms corresponding to each time step, and a constant factor weights each term.

$$\mathcal{L}_{VLB} = \mathbb{E}_{x, y_0, \epsilon} \left[\sum_{t=1}^T \frac{1}{T} \left\| \epsilon - \epsilon_\theta \left(x, \sqrt{\psi_t} y_0 + \sqrt{1 - \psi_t} \epsilon, \psi_t \right) \right\|_2^2 \right] \quad (18)$$

In this equation, ϵ represents a random variable that follows a standard normal distribution with mean 0 and identity covariance matrix I . It's important to note that this objective function is equivalent to the L_2 norm. Additionally, the distribution $p(\psi)$ is characterized as a uniform distribution over ψ_1, \dots, ψ_T .

Variogram-based Regularization: To further exhibit Ki-CDPM towards spatial dependence structure as the observed finer-resolution data (x_0) , we introduce **variogram-based regularization** in conjunction to Conditional Variational Lower Bound (\mathcal{L}_{VLB}). The regularization term \mathcal{R}_V penalizes the discrepancy between the *empirical* variogram of the generated noisy elevation maps (in the reverse process) and the variogram from the observed high-resolution map.

Let $\Delta_{x_t}(\mathbf{h})$ denote the empirical variogram of the generated elevation map x_t at step t , calculated as:

$$\Delta_{x_t}(\mathbf{h}) = \frac{1}{2|\mathcal{N}(\mathbf{h})|} \sum_{(s_i, s_j) \in \mathcal{N}(\mathbf{h})} (x_t(s_i) - x_t(s_j))^2 \quad (19)$$

where $\mathcal{N}(\mathbf{h})$ is the set of location pairs separated by the lag vector \mathbf{h} , and $|\cdot|$ denotes the cardinality of a set.

Let $\Delta_{x_0}(\mathbf{h})$ denote the variogram of the observed map (x_0) evaluated at lag \mathbf{h} :

$$\Delta_{x_0}(\mathbf{h}) = \frac{1}{2|\mathcal{N}(\mathbf{h})|} \sum_{(s_i, s_j) \in \mathcal{N}(\mathbf{h})} (x_0(s_i) - x_0(s_j))^2 \quad (20)$$

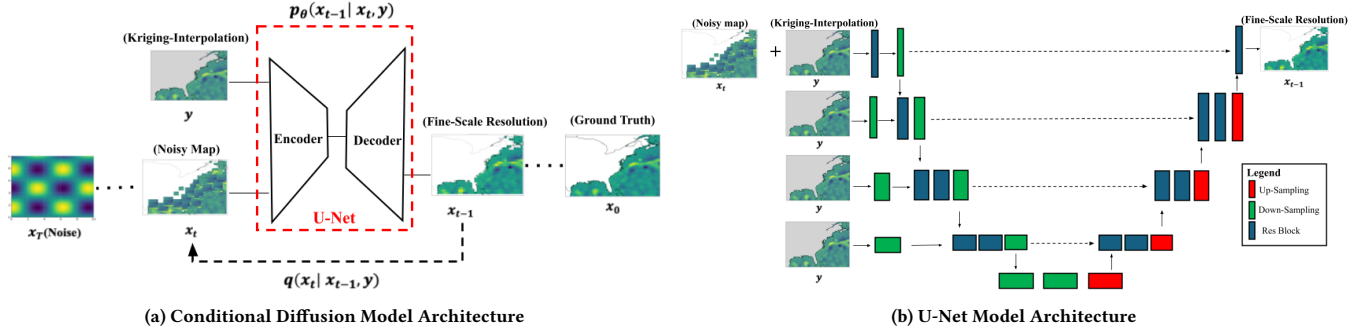


Figure 5: Proposed Kriging-informed Conditional Diffusion Model (Ki-CDPM) Architecture

Algorithm 3 Training in Ki-CDPM

```

1: repeat
2:    $(\mathbf{x}_0, \tilde{\mathbf{y}}) \sim p(\mathbf{x}, \tilde{\mathbf{y}})$ 
3:    $t \sim \text{Uniform}\{1, \dots, T\}$ 
4:    $\psi \sim p(\psi)$ 
5:    $\epsilon \sim \mathcal{N}(\mathbf{0}, \mathbf{I})$ 
6:    $\mathbf{y} \leftarrow \text{U-Krig}(\tilde{\mathbf{y}})$ 
7:   Compute  $\Delta_{\mathbf{x}_t}(\mathbf{h})$  and  $\Delta_{\mathbf{x}_0}(\mathbf{h})$ 
8:    $\mathcal{R}_V = \frac{1}{|\mathcal{H}|} \sum_{\mathbf{h} \in \mathcal{H}} (\Delta_{\mathbf{x}_t}(\mathbf{h}) - \Delta_{\mathbf{x}_0}(\mathbf{h}))^2$ 
9:   Take a gradient descent step on
    $\nabla_{\theta} \left\| \epsilon - f_{\theta}(\sqrt{\psi_t} \mathbf{x}_0 + \sqrt{1 - \psi_t} \epsilon, \mathbf{y}, t) \right\|^2 + \lambda_V \mathcal{R}_V$ 
10: until converged

```

The variogram-based regularization term \mathcal{R}_V is defined as the mean squared error between the empirical and observed variograms over a set of representative lag vectors \mathcal{H} :

$$\mathcal{R}_V = \frac{1}{|\mathcal{H}|} \sum_{\mathbf{h} \in \mathcal{H}} (\Delta_{\mathbf{x}_t}(\mathbf{h}) - \Delta_{\mathbf{x}_0}(\mathbf{h}))^2 \quad (21)$$

The regularization term \mathcal{R}_V is added to the original loss function of the CDPM, weighted by a hyperparameter λ_V :

$$\mathcal{L}_{\text{Ki-CDPM}} = \mathcal{L}_{\text{VLB}} + \lambda_V \mathcal{R}_V \quad (22)$$

The hyperparameter λ_V controls the strength of the variogram-based regularization and can be tuned to balance the trade-off between data fidelity and spatial structure preservation.

By minimizing the augmented loss function $L_{\text{Ki-CDPM}}$, the Ki-CDPM is encouraged to generate high-resolution elevation maps that match the finer-resolution observations and exhibit similar spatial dependence structures. Algorithm 3 provides training for Ki-CDPM in detail.

Once the Kriging-informed Conditional Diffusion Probabilistic Model (Ki-CDPM) has been trained, it can be used for inference to generate high-resolution sea-level elevation maps from coarse-resolution inputs. The inference involves applying the learned reverse diffusion process to a given coarse-resolution map (as a conditional input) to obtain a detailed, spatially coherent high-resolution map. Algorithm 4 describes the steps involved in the inference process and discusses generating high-resolution sea-level elevation maps using the Ki-CDPM.

Algorithm 4 Inference in Ki-CDPM

```

1:  $\mathbf{x}_T \sim \mathcal{N}(\mathbf{0}, \mathbf{I})$ 
2:  $\mathbf{y} \leftarrow \text{U-Krig}(\tilde{\mathbf{y}})$ 
3: for  $t = T, \dots, 1$  do
4:    $\mathbf{z} \sim \mathcal{N}(\mathbf{0}, \mathbf{I})$  if  $t > 1$ , else  $\mathbf{z} = \mathbf{0}$ 
5:    $\mathbf{x}_{t-1} = \frac{1}{\sqrt{\alpha_t}} \left( \mathbf{x}_t - \frac{1 - \alpha_t}{\sqrt{1 - \psi_t}} f_{\theta}(\mathbf{x}_t, \mathbf{y}, \psi_t) \right) + \sqrt{1 - \alpha_t} \mathbf{z}$ 
6: return  $\mathbf{x}_0$ 

```

4 Experimental Evaluation

Experimental Goal: Our experimental goal was to compare the solution quality of downscaling from our proposed Ki-CDPM model against state-of-the-art downscaling methods and provide both qualitative and quantitative analysis.

4.1 Experiment Design

Datasets: Our experimental evaluation focused on downscaling two key climate variables: sea-level anomaly (SLA) and eddy kinetic energy (EKE). We use high-resolution Copernicus and CMIP6 datasets and examined various sub-regions, including Eastern North America (ENA), western North America (WNA), and the Bay of Bengal (BoB) [17], an area particularly vulnerable to coastal flooding, due to the absence of ground truth data for climate models and the need for bias correction. We tested our methodology on satellite observations where the ground truth is known. Climate model outputs on sea level change are biased in the mean and variability, and the ground truth is unknown for high-resolution sea level values. Hence, we did not downscale climate model output in this study. Future studies will utilize high-resolution climate model outputs for training datasets as these high-resolution models are currently being tested[6].

The Copernicus Climate Data Store (CDS) dataset offers comprehensive global sea level anomaly data derived from satellite altimetry measurements. This dataset spans from 1993 to now and provides daily and monthly mean estimates of sea level anomalies. These anomalies are calculated with respect to a twenty-year reference sea level using absolute standards. The data is essential for monitoring the long-term evolution of sea levels and analyzing ocean and climate indicators. It includes sea level anomalies, absolute dynamic topography, and geostrophic velocities, which are crucial for approximating ocean surface currents. The dataset is

updated approximately three times a year with a delay of about five months to ensure accuracy and stability [44, 45].

The CMIP6 HighResMIP versions of EC-Earth provide global high-resolution coupled climate data developed by the EC-Earth consortium. The dataset includes EC-Earth3P-HR, with a high resolution of approximately 40 km for the atmosphere and 0.25 degrees for the ocean, and a standard-resolution version, EC-Earth3P, with 80 km for the atmosphere and 1.0 degrees for the sea. These are part of the High-Resolution Model Intercomparison Project (HighResMIP) and are designed to improve the accuracy of climate simulations by using higher resolutions. The high resolution enhances the representation of certain climate phenomena like the El Niño–Southern Oscillation, although it does not universally reduce biases in all regions [4].

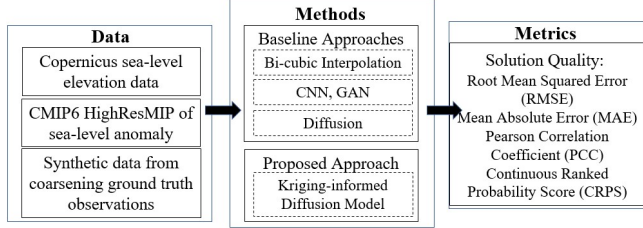


Figure 6: Experiment Design

Training & Inference: The model was trained on monthly mean data for both climate variables (sla, eke) in each of the three regions (ENA, WNA, BoB) for the duration from 1993-02 to 2013-12. The range of years for evaluation spans from 2014-01 to 2023-05. The data was transformed to the range [-1,1] to facilitate training convergence. We fixed $T = 1000$ for all experiments to align the number of neural network evaluations during sampling with those in prior studies [15, 41, 42]. The variances in the forward process were set to constants that increase linearly from $\beta_1 = 10^{-4}$ to $\beta_T = 0.02$. These values were selected to be small in comparison to the data scaled to the range [-1, 1], ensuring that the reverse and forward processes have roughly the same functional form while maintaining the signal-to-noise ratio at x_T as low as possible.

Evaluation Metrics: We assess model performance using standard downscaling evaluation metrics: root mean square error (RMSE), mean absolute error (MAE), and Pearson correlation coefficient (PCC). Additionally, we employed the continuous ranked probability score (CRPS) to evaluate the uncertainty inherent in the multiple predictions generated by diffusion models due to sampling from the terminal Gaussian distribution x_T . As only the traditional diffusion model in our baseline models produces probabilistic predictions, CRPS was used exclusively for comparison with this model.

Continuous Ranked Probability Score (CRPS):

$$\text{CRPS}(F, x) = \int_{-\infty}^{\infty} (F(y) - 1\{y \geq x\})^2 dy \quad (23)$$

where $1\{\cdot\}$ is the indicator function. CRPS [13] is employed to evaluate the accuracy and reliability of probabilistic forecasts in our downscaling model. CRPS measures the difference between the cumulative distribution function (CDF) of the predicted probability distribution F and the CDF of the observed value x . A lower CRPS value indicates a forecast that closely matches the observed outcomes, effectively capturing the uncertainty and variability in the

predictions. This metric is beneficial since it provides a comprehensive measure of forecast quality, encompassing both the accuracy and sharpness of the probabilistic predictions. Figure 6 shows the overall experiment design.

4.2 Experimental Results

Quantitative results: Results averaged over the entire test dataset for Sea-level Anomaly (SLA) in the Eastern North America (ENA) region are presented in Tables 3, 4, and 5. The quantitative evaluation of the Ki-CDPM model demonstrates its superior performance compared to state-of-the-art baseline methods for sea-level elevation downscaling. Table 3 presents a comprehensive comparison using RMSE, MAE, and PCC metrics across three regions: Eastern North America (ENA), Western North America (WNA), and the Bay of Bengal (BoB). Ki-CDPM consistently achieves the lowest RMSE and MAE values and the highest PCC values among all methods, indicating its ability to generate accurate and spatially consistent downscaled data. The lower RMSE and MAE values indicate higher accuracy in predicting sea-level elevation. In contrast, the elevated PCC value further suggests that the predicted elevations closely align with the patterns and trends observed in the ground truth data, highlighting the model's ability to accurately capture the spatial variability and gradients inherent in sea-level elevations.

Specifically, in the ENA region, Ki-CDPM obtains an RMSE of 1.1, MAE of 0.8, and PCC of 0.94, outperforming the best-performing baseline, the diffusion-based downscaling method, which yields an RMSE of 2.5, MAE of 1.9, and PCC of 0.91. Similar trends are observed in the WNA and BoB regions, where Ki-CDPM maintains its superiority across all metrics. Table 4 compares the performance of Ki-CDPM with the diffusion-based downscaling method using the CRPS metric, which assesses the accuracy and reliability of probabilistic predictions. Ki-CDPM achieves lower CRPS values in all three regions (0.09 for ENA, 0.22 for WNA, and 0.31 for BoB) compared to the diffusion-based method (0.13 for ENA, 0.31 for WNA, and 0.37 for BoB), further confirming its ability to provide more accurate and reliable probabilistic downscaling data.

Additionally, an ablation study presented in Table 5 highlights the impact of the variogram regularizer in Ki-CDPM. The inclusion of the regularizer leads to improved performance across all metrics in the ENA region, with an RMSE of 1.1, MAE of 0.8, PCC of 0.94, and CRPS of 0.09, compared to the model without the regularizer (RMSE of 1.3, MAE of 1.0, PCC of 0.92, and CRPS of 0.11). These results underscore the importance of the variogram-based regularizer in enhancing the accuracy and reliability of the Ki-CDPM model for sea-level elevation downscaling.

In addition to downscaling sea-level elevation, the Ki-CDPM model demonstrates superior performance in downscaling other climate variables, such as eddy kinetic energy (EKE), as shown in Tables 6, 7, and 8. Ki-CDPM achieves the lowest RMSE, MAE, and CRPS values and the highest PCC values compared to baseline methods across Eastern North America (ENA), Western North America (WNA), and Bay of Bengal (BoB) regions. Specifically, in the ENA region, Ki-CDPM with variogram regularizer achieves an RMSE of 194.83, MAE of 158.62, PCC of 0.95, and CRPS of 0.08, significantly outperforming the model without the regularizer. These results highlight the versatility and robustness of Ki-CDPM in accurately downscaling diverse climate variables.

Table 3: Performance comparison of Ki-CDPM and baseline methods using RMSE, MAE, and PCC on sea-level elevation.

Model	Eastern North America (ENA)			Western North America (WNA)			Bay of Bengal (BoB)		
	RMSE↓	MAE↓	PCC↑	RMSE↓	MAE↓	PCC↑	RMSE↓	MAE↓	PCC↑
Bicubic Interpolation	18.7	14.8	0.72	25.1	18.3	0.68	29.7	22.9	0.65
CNN-based Downscaling [49]	6.3	5.6	0.81	11.4	8.8	0.78	13.4	11.8	0.74
GAN-based Downscaling [11]	4.8	4.1	0.87	8.3	6.2	0.81	9.8	8.3	0.78
Baseline Diffusion Downscaling [53]	2.5	1.9	0.91	4.6	3.4	0.87	6.1	5.1	0.82
Ki-CDPM	1.1	0.8	0.94	2.4	2.1	0.91	4.0	3.2	0.86

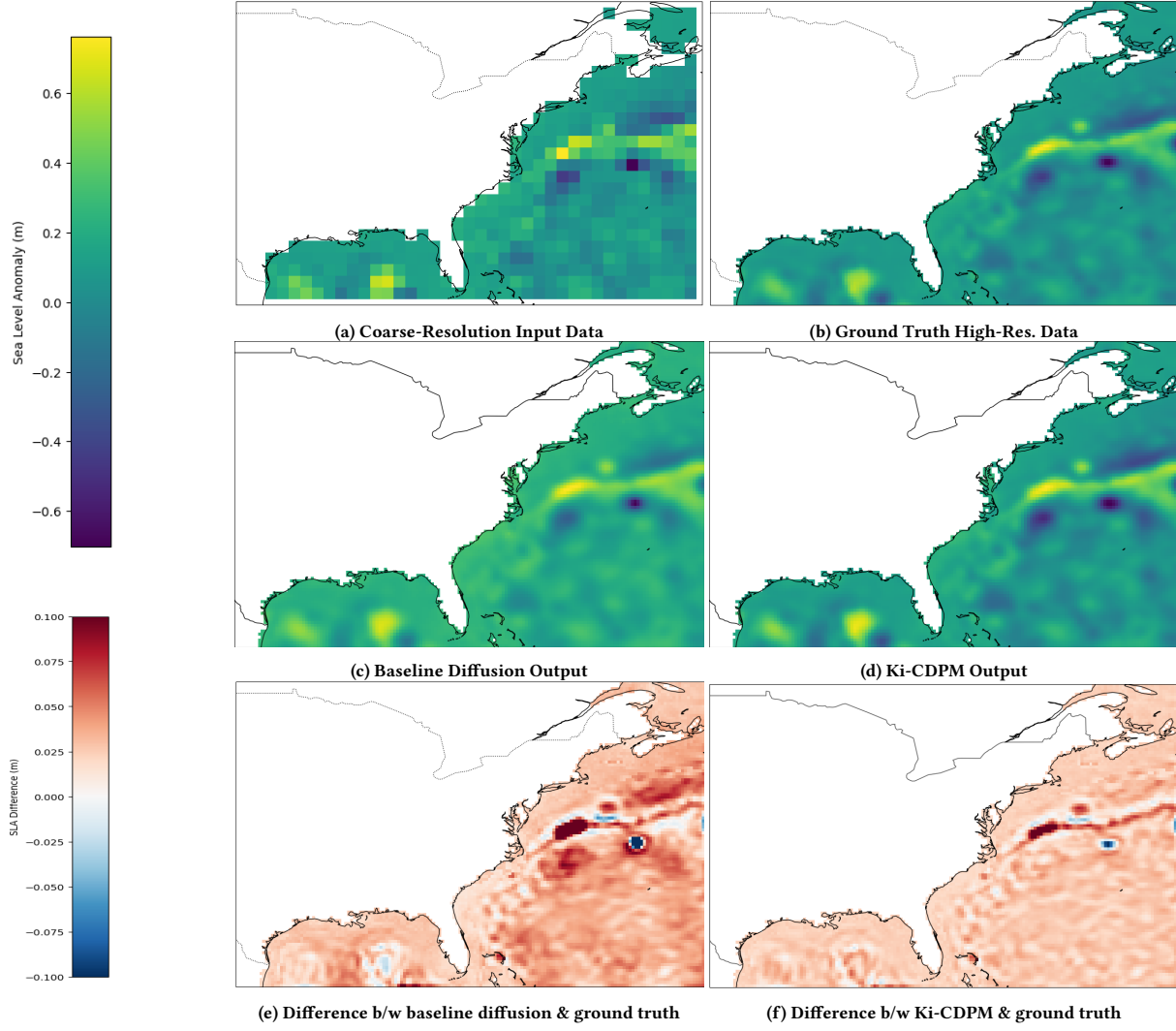


Figure 7: Qualitative Analysis on sea-level elevation in ENA region (Best in color).

Table 4: Performance comparison of Ki-CDPM and baseline methods using CRPS on sea-level elevation .

Model	CRPS↓		
	ENA	WNA	BoB
Baseline Diffusion Downscaling	0.13	0.31	0.37
Ki-CDPM	0.09	0.22	0.31

Table 5: Ablation study on the impact of variogram regularizer in Ki-CDPM on sea-level elevation in Eastern North America (ENA).

Method	RMSE↓	MAE↓	PCC↑	CRPS↓
Ki-CDPM (w variogram)	1.1	0.8	0.94	0.09
Ki-CDPM (w/o variogram)	1.3	1.0	0.92	0.11

Qualitative results: Figure 7 illustrates the comparative performance of Ki-CDPM against the ground truth and baseline diffusion

Table 6: Performance comparison of Ki-CDPM and baseline methods using RMSE, MAE, and PCC on eddy kinetic energy (EKE).

Model	Eastern North America (ENA)			Western North America (WNA)			Bay of Bengal (BoB)		
	RMSE↓	MAE↓	PCC↑	RMSE↓	MAE↓	PCC↑	RMSE↓	MAE↓	PCC↑
Bicubic Interpolation	1524.67	1207.52	0.71	1762.34	1415.88	0.67	1985.19	1603.27	0.64
CNN-based Downscaling	752.14	621.87	0.82	869.42	733.64	0.77	1052.76	895.41	0.74
GAN-based Downscaling	493.58	425.36	0.86	647.25	557.43	0.82	751.09	663.71	0.79
Baseline Diffusion Downscaling	266.27	219.84	0.92	411.92	347.66	0.88	486.91	419.52	0.83
Ki-CDPM	194.83	158.62	0.95	293.51	246.83	0.91	354.07	301.14	0.86

Table 7: Performance comparison of Ki-CDPM and baseline methods using CRPS on eddy kinetic energy (EKE).

Model	CRPS↓		
	ENA	WNA	BoB
Baseline Diffusion Downscaling	0.14	0.30	0.39
Ki-CDPM	0.08	0.23	0.30

Table 8: Ablation study on the impact of variogram regularizer in Ki-CDPM on eddy kinetic energy (EKE) in Eastern North America (ENA).

Method	RMSE↓	MAE↓	PCC↑	CRPS↓
Ki-CDPM w/ variogram	194.83	158.62	0.95	0.08
Ki-CDPM (w/o variogram)	250.25	198.27	0.93	0.11

model for sea-level elevation at a single timestep. The baseline model, conditioned on bicubic interpolation of coarse data, exhibits limitations in predicting values closer to the coastline and produces some pixelated artifacts. In contrast, Ki-CDPM leverages the spatial dependency structure provided by Kriging and the variogram, resulting in superior downscaling with finer details and improved accuracy. Resolving these fine-scale structures and gradients in sea-level elevation is essential to predict better regional impacts of sea-level rise and better model spatial variability in sea-level elevation. The fine-scale eddy features seen in the downsampled maps of sea level elevation play a crucial role in ocean dynamics and the evolution of the ocean fields. The 1 deg coarse resolution model outputs, which is the typical resolution of current generation climate models, do not resolve these features in the ocean. Hence, resolving them and seeing their evolution in time helps predict the changes to ocean circulation and their impact on rising sea levels in coastal communities.

In the study, the satellite observed a high-resolution sea-level elevation map at 0.25 degrees resolution, which serves as the accuracy benchmark, while a coarser 1-degree resolution map is utilized as input data. The main text compares the proposed method's performance with a state-of-the-art traditional diffusion model, showcasing qualitative results.

5 Related Work

Spatial variability [9] is a significant characteristic of all geographic phenomena, such as climate zones, USDA plant hardiness zones [47], and different terrestrial habitats like forests, grasslands, wetlands, and deserts. This variability influences the flora and fauna within different regions. Additionally, variations in laws, policies, and cultural norms are evident across and within nations. Often

referred to as geography's second law, spatial variability is utilized in analytical models like geographically weighted regression (GWR) [29] to measure the interactions between variables in a given area. The challenge of quantifying spatial variability stems from many geophysical elements affecting it. Soil scientists, for example, study soil attributes such as carbon content to evaluate agricultural yield and have noted considerable variation in soil samples within a mere 100 m² due to aspects like tillage, soil makeup, vegetation, land management, and topography. Anomaly detection [1] has been widely studied in spatial data mining (e.g., trajectory gaps [37–39]). However, only a limited number of statistical [7] and machine learning methods have addressed anomaly detection in climate science.

Traditional machine learning models [30], primarily designed for image processing, encounter several obstacles, including the absence of physical constraints, difficulties with managing high-dimensional climate data, and their inability to yield probabilistic outputs in climate data. For instance, Autoregressive models (ARs) [36, 48] are capable of model log-likelihood and complex distributions. Variational Autoencoders (VAEs) [20, 33] provide rapid sampling capabilities. Generative Adversarial Networks (GANs) [8] favored for tasks like class-conditional image generation etc. Climate downscaling [12, 19, 25, 26] is widely used to facilitate understanding and planning for climate impacts at regional or local levels, with machine learning models also applied in statistical downscaling [22]. Recently, diffusion models have gained interest in climate science due to their capacity to model non-linear relationships, although they struggle with generalization, maintaining physical consistency, and non-stationarity. For example, [51, 53] overlook spatial dependencies, leading to inaccurate depictions of physical processes like ocean currents, wind patterns, and temperature gradients. This work introduces Ki-CDPM, incorporating geostatistical capabilities with a Conditional Diffusion Model to effectively capture spatial variability in climate model variables such as sea level rise.

Domain Background: The SWOT (Surface Water and Ocean Topography) [43] satellite mission offers significant advancements over the TOPEX/Poseidon mission in measuring sea level and surface water elevation. While TOPEX provided accurate ocean surface topography data, SWOT extends this capability to measure ocean and freshwater bodies with unprecedented detail. SWOT's higher-resolution measurements enable precise monitoring of smaller-scale ocean phenomena and inland water bodies, which is crucial for understanding climate change impacts. Its innovative Ka-band Radar Interferometer delivers finer spatial resolution, enhancing our ability to track water storage and movement changes. This comprehensive data set supports improved global water resource

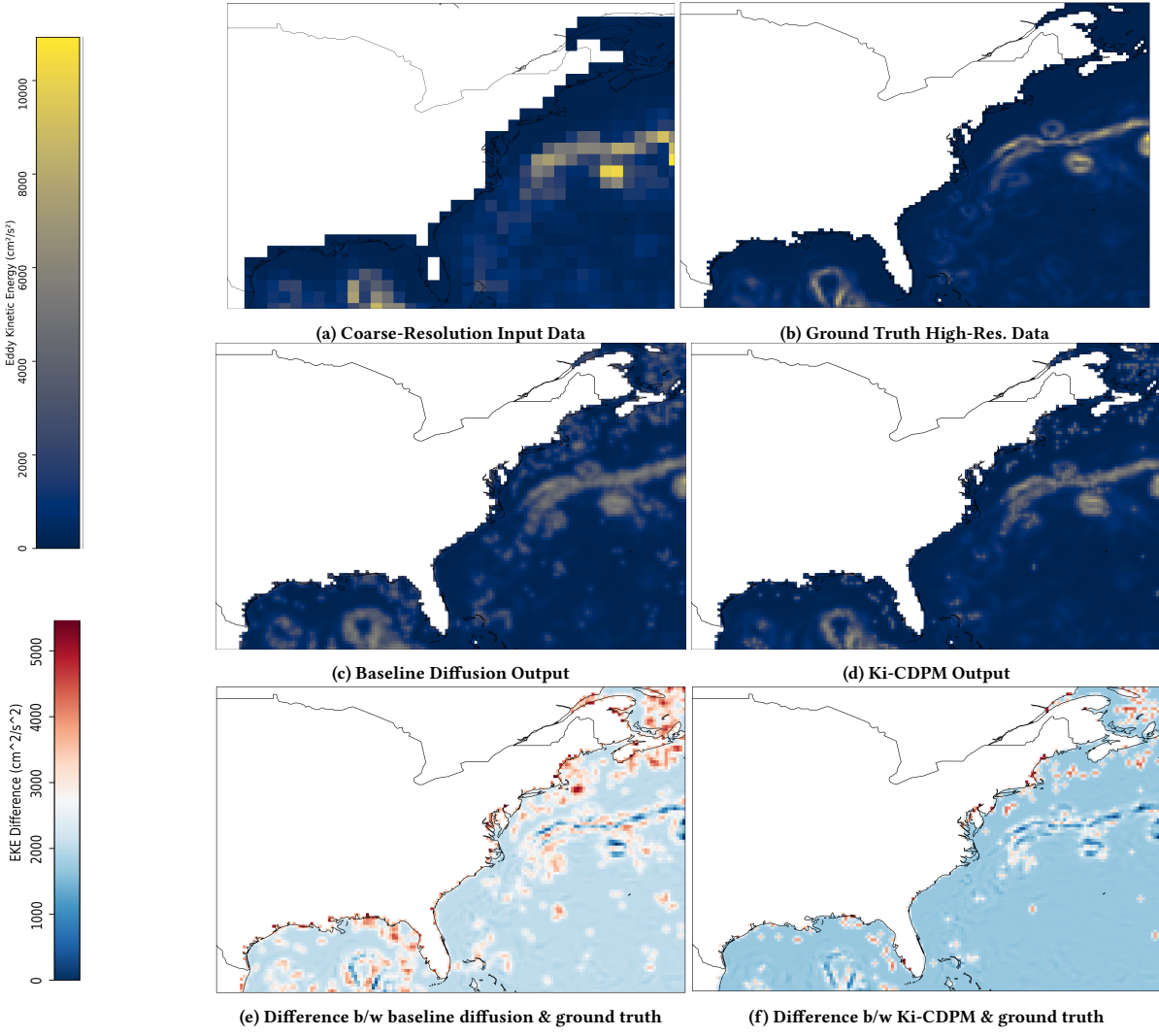


Figure 8: Qualitative Analysis on eddy kinetic energy (EKE) in ENA region (Best in color).

management, disaster response, and climate prediction models, addressing modern environmental challenges through advanced computational analysis.

6 Conclusion and Future Work

We proposed the Kriging-Informed Conditional Diffusion Probabilistic Model (Ki-CDPM) to address the challenge of downscaling sea-level elevation data from coarse to fine resolution. We further integrated Universal Kriging via the Matérn variogram model with the Conditional Diffusion Probabilistic Model (CDPM), leveraging the strength of geostatistical interpolation to enhance the resolution and realism of downscaled data. Experimental results demonstrate that Ki-CDPM outperforms state-of-the-art methods, generating high-resolution sea-level projections essential for regional climate impact assessments and coastal management.

Future Work: We will explore the application of the Ki-CDPM to other climate variables, such as temperature and precipitation, to evaluate its versatility and robustness across different datasets.

Investigating additional geostatistical models could further improve the quality and diversity of the generated outputs. Moreover, developing strategies incorporating domain knowledge such as ocean bed topology and mass balance will be beneficial. Finally, we plan to optimize the computational efficiency of the diffusion model by using novel sampling methods to reduce its computational demands.

7 Acknowledgments

This material is based upon work supported by the National Science Foundation under Grants No. 2118285, approved for public release, 22-536. We also want to thank Kim Koffolt and the spatial computing research group for their helpful comments and refinements. We also thank NCAR for computing resources.

References

- [1] Varun Chandola, Arindam Banerjee, and Vipin Kumar. 2009. Anomaly detection: A survey. *ACM computing surveys (CSUR)* 41, 3 (2009), 1–58.
- [2] Nanxin Chen, Yu Zhang, Heiga Zen, Ron J. Weiss, Mohammad Norouzi, and William Chan. 2021. WaveGrad: Estimating Gradients for Waveform Generation.

In *International Conference on Learning Representations (ICLR)*. PMLR, Virtual Conference, 1–10. <https://openreview.net/forum?id=NsMLjcFaO0>

[3] John A. Church, Peter U. Clark, Anny Cazenave, Jonathan M. Gregory, Svetlana Jevrejeva, Anders Levermann, Mark A. Merrifield, Glenn A. Milne, R. Steven Nerem, and Patrick D. Nunn. 2013. Sea Level Change. In *Climate Change 2013: The Physical Science Basis. Contribution of Working Group I to the Fifth Assessment Report of the Intergovernmental Panel on Climate Change*. Cambridge University Press, Cambridge, United Kingdom, 1137–1216. <https://doi.org/10.1017/CBO9781107415324.026>

[4] Rein Haarsma et al. 2020. HighResMIP versions of EC-Earth: EC-Earth3P and EC-Earth3P-HR – description, model computational performance and basic validation. *Geoscientific Model Development* 13 (2020), 3507–3527. <https://doi.org/10.5194/gmd-13-3507-2020>

[5] Andra J. Garner, Jeremy L. Weiss, Adam Parris, Robert E. Kopp, Radley M. Horton, Jonathan T. Overpeck, and Benjamin P. Horton. 2018. Evolution of 21st Century Sea Level Rise Projections. *Earth's Future* 6, 11 (2018), 1603–1615. <https://doi.org/10.1029/2018EF000859>

[6] Estibaliz Gascón, Irina Sandu, Benoît Vannière, Linus Magnusson, Richard Forbes, Inna Polichtchouk, Annelie Van Niekerk, Birgit Stütz, Michael Maier-Gerber, Michail Diamantakis, Peter Bechtold, and Giampaolo Balsamo. 2023. Advances Towards a Better Prediction of Weather Extremes in the Destination Earth Initiative. In *EMS Annual Meeting 2023*. Copernicus Meetings, Copernicus GmbH, Bratislava, Slovakia, 1–2. Abstract.

[7] Subhankar Ghosh, Jayant Gupta, Arun Sharma, Shuai An, and Shashi Shekhar. 2022. Towards geographically robust statistically significant regional colocation pattern detection. In *Proceedings of the 5th ACM SIGSPATIAL International Workshop on GeoSpatial Simulation*, 11–20.

[8] Ian Goodfellow, Jean Pouget-Abadie, Mehdi Mirza, Bing Xu, David Warde-Farley, Sherjil Ozair, Aaron Courville, and Yoshua Bengio. 2014. Generative Adversarial Networks. In *Advances in Neural Information Processing Systems (NeurIPS)*, Vol. 27. Curran Associates, Inc., Montreal, Canada, 2672–2680.

[9] Jayant Gupta, Carl Molnar, Yiqun Xie, Joe Knight, and Shashi Shekhar. 2021. Spatial variability aware deep neural networks (svann): A general approach. *ACM Transactions on Intelligent Systems and Technology (TIST)* 12, 6 (2021), 1–21.

[10] Benjamin D Hamlington, Alex S Gardner, Erik Ivins, Jan TM Lenaerts, JT Reager, David S Trossman, Edward D Zaron, Surendra Adhikari, Anthony Arendt, Andy Aschwanden, et al. 2020. Understanding of Contemporary Regional Sea-Level Change and the Implications for the Future. *Reviews of Geophysics* 58, 3 (2020), e2019RG000672. <https://doi.org/10.1029/2019RG000672>

[11] Lucy Harris et al. 2022. A Generative Deep Learning Approach to Stochastic Downscaling of Precipitation Forecasts. *Journal of Advances in Modeling Earth Systems* 14 (2022), e2022MS003178. <https://doi.org/10.1029/2022MS003178>

[12] Tim HJ Hermans, Jonathan Tinker, Matthew D Palmer, Caroline A Katsman, Bert LA Vermeersen, and Aimée BA Slanen. 2020. Improving sea-level projections on the Northwestern European shelf using dynamical downscaling. *Climate Dynamics* 54, 3 (2020), 1987–2011.

[13] Hans Hersbach. 2000. Decomposition of the continuous ranked probability score for ensemble prediction systems. *Weather and Forecasting* 15, 5 (2000), 559–570.

[14] Jonathan Ho, Ajay Jain, and Pieter Abbeel. 2020. Denoising diffusion probabilistic models. In *Proceedings of the 34th International Conference on Neural Information Processing Systems (Vancouver, BC, Canada) (NIPS '20)*. Curran Associates Inc., Red Hook, NY, USA, Article 574, 12 pages.

[15] Jonathan Ho, Ajay Jain, and Pieter Abbeel. 2020. Denoising Diffusion Probabilistic Models. In *Advances in Neural Information Processing Systems*, Vol. 33. Curran Associates, Inc., Vancouver, Canada, 6840–6851.

[16] Intergovernmental Panel on Climate Change (IPCC). 2021. Climate Change 2021: The Physical Science Basis. Contribution of Working Group I to the Sixth Assessment Report of the Intergovernmental Panel on Climate Change. Chapter 10: Linking Global to Regional Climate Change. https://www.ipcc.ch/report/ar6/wg1/downloads/report/IPCC_AR6_WGI_Chapter10.pdf Accessed: 2024-06-06.

[17] M. Iturbide et al. 2020. An Update of IPCC Climate Reference Regions for Subcontinental Analysis of Climate Model Data: Definition and Aggregated Datasets. *Earth System Science Data* 12 (2020), 2959–2970. <https://doi.org/10.5194/essd-12-2959-2020>

[18] Shanhui Jiang et al. 2020. Downscaling and projection of multi-CMIP5 precipitation using machine learning methods in the Upper Han River Basin. *Atmospheric Research* 247 (2020), 105156.

[19] Yong-Yub Kim et al. 2021. Local Sea-level rise caused by climate change in the Northwest pacific marginal seas using dynamical downscaling. *Frontiers in Marine Science* 8 (2021), 620570.

[20] Diederik P. Kingma and Max Welling. 2014. Auto-Encoding Variational Bayes. In *International Conference on Learning Representations (ICLR)*. PMLR, Banff, Canada, 1–10. Available at <https://arxiv.org/abs/1312.6114>.

[21] Robert E. Kopp, Radley M. Horton, Christopher M. Little, Jerry X. Mitrovica, Michael Oppenheimer, D.J. Rasmussen, Benjamin H. Strauss, and Claudia Tebaldi. 2014. Probabilistic 21st and 22nd Century Sea-Level Projections at a Global Network of Tide-Gauge Sites. *Earth's Future* 2, 8 (2014), 383–406. <https://doi.org/10.1002/2014EF000239>

[22] Jussi et. al Leinonen. 2020. Stochastic super-resolution for downscaling time-evolving atmospheric fields with a generative adversarial network. *IEEE Transactions on Geoscience and Remote Sensing* 59, 9 (2020), 7211–7223.

[23] X. Li et al. 2020. Performance of statistical and machine learning ensembles for daily temperature downscaling. *Theoretical and Applied Climatology* 140, 1 (2020), 1–17. <https://doi.org/10.1007/s00704-019-03028-1>

[24] Yijun Lin and Yao-Yi Chiang. 2023. Modeling Spatially Varying Physical Dynamics for Spatiotemporal Predictive Learning. In *Proceedings of the 31st ACM SIGSPATIAL International Conference on Advances in Geographic Information Systems (SIGSPATIAL)*. ACM, Hamburg, Germany, 98:1–98:11. <https://doi.org/10.1145/3589132.3625648>

[25] Xiaoyu Liu et al. 2022. Downscaling of Climate Model Projections for Sea Level Rise Assessments: A Review. *Journal of Geophysical Research: Oceans* 127, 4 (2022), e2021JC018048. <https://doi.org/10.1029/2021JC018048>

[26] Zhao-Jun Liu, Shoshiro Minobe, Yoshi N Sasaki, and Mio Terada. 2016. Dynamical downscaling of future sea level change in the western North Pacific using ROMS. *Journal of Oceanography* 72 (2016), 905–922.

[27] Douglas Maraun, Martin Widmann, José M Gutiérrez, Radan Huth, Elke Hertig, Rasmus Benestad, Ole Roessler, Pedro M M Soares, José M Diaz-Navarro, Eva Enkelmann, et al. 2018. Statistical downscaling skill under present climate conditions: A synthesis of the VALUE perfect predictor experiment. *International Journal of Climatology* 39, 9 (2018), 3692–3703.

[28] Gordon McGranahan, Deborah Balk, and Bridget Anderson. 2007. The Rising Tide: Assessing the Risks of Climate Change and Human Settlements in Low Elevation Coastal Zones. *Environment and Urbanization* 19, 1 (2007), 17–37. <https://doi.org/10.1177/0956247807076960>

[29] Daniel P McMillen. 2004. Geographically weighted regression: the analysis of spatially varying relationships.

[30] Himadri Mukherjee, Subhankar Ghosh, Shibaprasad Sen, Obaidullah Sk Md, KC Santosh, Santanu Phadikar, and Kaushik Roy. 2019. Deep learning for spoken language identification: Can we visualize speech signal patterns? *Neural Computing and Applications* 31 (2019), 8483–8501.

[31] Michael Oppenheimer et al. 2019. Sea Level Rise and Implications for Low-Lying Islands, Coasts and Communities. IPCC Special Report on the Ocean and Cryosphere in a Changing Climate, Chapter 4. <https://www.ipcc.ch/srocc/chapter/chapter-4-a-sea-level-rise-and-implications-for-low-lying-islands-coasts-and-communities/>

[32] Hannah S. Rabinowitz, Sophia Dahodwala, Sophie Baur, and Alison Delgado. 2023. Availability of State-level Climate Change Projection Resources for Use in Site-level Risk Assessment. *Frontiers in Environmental Science* 11 (2023), Article 1206039. <https://doi.org/10.3389/fenvs.2023.1206039>

[33] Danilo Jimenez Rezende, Shakir Mohamed, and Daan Wierstra. 2014. Stochastic Backpropagation and Approximate Inference in Deep Generative Models. In *Proceedings of the 31st International Conference on Machine Learning (ICML)*. PMLR, Beijing, China, 1278–1286.

[34] Olaf Ronneberger, Philipp Fischer, and Thomas Brox. 2015. U-Net: Convolutional Networks for Biomedical Image Segmentation. In *International Conference on Medical Image Computing and Computer-Assisted Intervention (MICCAI)*. Springer, Munich, Germany, 234–241. https://doi.org/10.1007/978-3-319-24574-4_28

[35] Raina M Rutti, Fernando Garcia, and Marilyn M Helms. 2021. Entrepreneurship in Peru: a SWOT analysis. *International Journal of Entrepreneurship and Small Business* 42, 3 (2021), 369–396.

[36] Tim Salimans, Andrej Karpathy, Xi Chen, and Diederik P. Kingma. 2017. Pixel-CNN++: Improving the PixelCNN with Discretized Logistic Mixture Likelihood and Other Modifications. [arXiv:1701.05517 \[cs.LG\]](https://arxiv.org/abs/1701.05517) <https://arxiv.org/abs/1701.05517>

[37] Arun Sharma, Subhankar Ghosh, and Shashi Shekhar. 2024. Physics-based Abnormal Trajectory Gap Detection. *ACM Transactions on Intelligent Systems and Technology* (2024).

[38] Arun Sharma, Jayant Gupta, and Subhankar Ghosh. 2022. Towards a tighter bound on possible-rendezvous areas: preliminary results. In *Proceedings of the 30th International Conference on Advances in Geographic Information Systems*, 1–11.

[39] Arun Sharma, Xun Tang, Jayant Gupta, Majid Farhadloo, and Shashi Shekhar. 2020. Analyzing trajectory gaps for possible rendezvous: A summary of results. In *11th International Conference on Geographic Information Science (GIScience 2021)-Part I*. Schloss Dagstuhl-Leibniz-Zentrum für Informatik.

[40] Aimée BA Slanen, Mark Carson, Caroline A Katsman, Roderik SW Van de Wal, Armin Köhl, LLA Vermeersen, and Detlef Stammer. 2014. Projecting twenty-first century regional sea-level changes. *Climatic Change* 124, 1 (2014), 317–332.

[41] Jascha Sohl-Dickstein, Eric Weiss, Niru Maheswaranathan, and Surya Ganguli. 2015. Deep Unsupervised Learning Using Nonequilibrium Thermodynamics. In *Proceedings of the 32nd International Conference on Machine Learning (ICML)*. PMLR, Lille, France, 2256–2265.

[42] Yang Song and Stefano Ermon. 2019. Generative Modeling by Estimating Gradients of the Data Distribution. In *Advances in Neural Information Processing Systems*. Curran Associates, Inc., Vancouver, Canada, 11918–11930.

[43] M. Srinivasan and V. Tsontos. 2023. Satellite Altimetry for Ocean and Coastal Applications: A Review. *Remote Sensing* 15, 16 (2023), 3939.

[44] Copernicus Climate Data Store. 2024. Climate Data. <https://cds.climate.copernicus.eu/portfolio/dataset/satellite-sea-surface-temperature> Accessed: 2024-05-28.

[45] Copernicus Climate Data Store. 2024. Sea Level Gridded Data from Satellite Observations. <https://cds.climate.copernicus.eu/portfolio/dataset/satellite-sea-level-global> Accessed: 2024-05-28.

[46] Claudia Teutschbein and Jan Seibert. 2012. Evaluation of different downscaling techniques for hydrological climate-change impact studies at the catchment scale. *Climate Dynamics* 37, 9 (2012), 2087–2105.

[47] USDA. 2012. USDA Plant Hardiness Zone Map. <https://planthardiness.ars.usda.gov/>. Accessed: 2021-04-26.

[48] Aäron Van Den Oord, Nal Kalchbrenner, and Koray Kavukcuoglu. 2016. Pixel Recurrent Neural Networks. In *Proceedings of the 33rd International Conference on Machine Learning (ICML) (ICML '16)*. JMLR.org, New York, NY, USA, 1747–1756.

[49] Thomas Vandal, Evan Kodra, Sangram Ganguly, Andrew Michaelis, Ramakrishna Nemani, and Auroop R. Ganguly. 2017. DeepSD: Generating High Resolution Climate Change Projections through Single Image Super-Resolution. In *Proceedings of the 23rd ACM SIGKDD International Conference on Knowledge Discovery and Data Mining (Halifax, NS, Canada) (KDD '17)*. Association for Computing Machinery, New York, NY, USA, 1663–1672. <https://doi.org/10.1145/3097983.3098004>

[50] Sergio M Vicente-Serrano et al. 2014. Improved statistical downscaling of climate scenarios using a three-step analogue regression downscaling method. *Journal of Geophysical Research: Atmospheres* 119, 17 (2014), 9539–9553.

[51] Zhong Yi Wan, Ricardo Baptista, Yi fan Chen, John Anderson, Anudhyan Boral, Fei Sha, and Leonardo Zepeda-Núñez. 2023. Debias Coarsely, Sample Conditionally: Statistical Downscaling through Optimal Transport and Probabilistic Diffusion Models. arXiv:2305.15618 [cs.LG] <https://arxiv.org/abs/2305.15618>

[52] Xiaolin Wang, Hui Wan, Shukun Jiao, Robert P. Allan, and Alison Pamment. 2021. Coastal Sea Level Changes and Extremes in a Warming Climate. *Journal of Climate* 34, 20 (2021), 8375–8393. <https://doi.org/10.1175/JCLI-D-21-0171.1>

[53] Robbie A. Watt and Laura A. Mansfield. 2024. Generative Diffusion-based Downscaling for Climate. arXiv:2404.17752 [physics.ao-ph] <https://arxiv.org/abs/2404.17752>

[54] Haomin Wen, Youfang Lin, Yutong Xia, Huaiyu Wan, Qingsong Wen, Roger Zimmermann, and Yuxuan Liang. 2023. DiffSTG: Probabilistic Spatio-Temporal Graph Forecasting with Denoising Diffusion Models. In *Proceedings of the 31st ACM International Conference on Advances in Geographic Information Systems (Hamburg, Germany) (SIGSPATIAL '23)*. Association for Computing Machinery, New York, NY, USA, Article 60, 12 pages. <https://doi.org/10.1145/3589132.3625614>

[55] Zhilun Zhou, Jingtao Ding, Yu Liu, Depeng Jin, and Yong Li. 2023. Towards Generative Modeling of Urban Flow through Knowledge-enhanced Denoising Diffusion. In *Proceedings of the 31st ACM International Conference on Advances in Geographic Information Systems (Hamburg, Germany) (SIGSPATIAL '23)*. Association for Computing Machinery, New York, NY, USA, Article 91, 12 pages. <https://doi.org/10.1145/3589132.3625641>